Triggered-bubble-chamber study of the reaction $\pi^+p \to \Delta^{++}\pi^0\pi^0$ at 16 GeV/c

R. K. Clark,* P. M. Barlow,† R. N. Diamond‡ V. Hagopian, J. E. Lannutti, and C. M. Spencer§
Florida State University, Tallahassee, Florida 32306

M. Ferguson, T. Glanzman,** A. T. Goshaw, P. Lucas,†† N. Morgan, W. Robertson, and W. D. Walker
Duke University, Durham, North Carolina 27706

W. Bugg, G. Condo, T. Handler, E. Hart, and A. Rogers
University of Tennessee, Knoxville Tennessee 37996

H. O. Cohn
Oak Ridge National Laboratory, Oak Ridge, Tennessee 37830

I. J. Kim, and C. R. Sun
State University of New York at Albany, Albany, New York 12203

R. Gearhart
Stanford Linear Accelerator Center, Stanford, California 94305
(Received 27 July 1984; revised manuscript received 6 May 1985)

The SLAC 40-inch bubble chamber augmented by an array of lead-glass detectors was used to study the reaction $\pi^+p \to \Delta^{++}\pi^0\pi^0$ at 15.7 GeV/c. No new high-mass neutral mesons are seen at a sensitivity of 14.2 events/μb. A moments and amplitude analysis indicates that only S and D waves contribute to the $\pi^+\pi^- \to \pi^0\pi^0$ cross section. A one-pion-exchange-model calculation is performed using phase-shift measurements from other experiments. The older phase shifts from Estabrooks and Martin are in better agreement with our data than are the more recent ones of Biswas *et al.*

I. INTRODUCTION

We report here the results of a study of the reaction

$$\pi^+p \to \pi^+p\pi^0\pi^0 \tag{1}$$

using the SLAC 40-in. hydrogen-filled bubble chamber. The bubble chamber was augmented by a downstream wall of lead glass[1,2] whose function was to detect the produced γ rays and to trigger the bubble-chamber cameras when sufficient energy was deposited. A downstream proportional-wire-chamber (PWC) system[3] was also used for triggering the cameras, and was capable of providing improved momentum measurements of the charged primary tracks.

The study of reaction (1) is virtually impossible in a bare bubble chamber because of the low-γ-ray conversion probability. Counter experiments which have good γ-ray detection efficiency have limited acceptance and may have background problems due to the inability to reconstruct all of the final-state particles. This experiment is a first attempt to overcome the limitations of the bare-bubble-chamber and purely electronic experiments.

In the next section we describe the experimental setup and in Sec. III the event-reconstruction procedures. In Sec. IV we discuss the reaction

$$\pi^+p \to \Delta^{++}\pi^0\pi^0 \tag{2}$$

and present results of our amplitude and phase-shift analysis of the process $\pi^+\pi^- \to \pi^0\pi^0$, which can be isolated in the reaction. We summarize our results in Sec. V.

II. EXPERIMENTAL SETUP

Figure 1 is a schematic diagram of the experimental setup used for experiment BC-67. The π^+ beam, defined by scintillator S1, Čerenkov counter CB, and beam hodoscope BH, was pinpointed by PWC1 and PWC2. Behind the bubble chamber were four sets of PWC planes which were part of the trigger and were used to identify γ-ray conversions in the exit window of the bubble chamber and to help in the extrapolation of charged tracks into the lead-glass wall. Two scintillators S3 and S4, located downstream of the bubble chamber, were used as beam veto counters.

The lead-glass wall[1,2] had an active converter of two columns each with 26 blocks, 10 cm$\times$10 cm$\times$90 cm stacked horizontally and perpendicular to the beam. The absorber blocks were 15.4 cm$\times$15.4 cm$\times$33 cm, stacked lengthwise to the beam in an array 8 across by 19 high. The middle 88 blocks (between rows 5 and 15 inclusive) were made into double blocks by gluing two absorber blocks end-to-end with RTV-type 615 cement. These double blocks were necessary in order to completely absorb the highest-energy photon showers. In front of the active converter was a 1-radiation-length-thick lead sheet, the purpose of which, was to maximize the

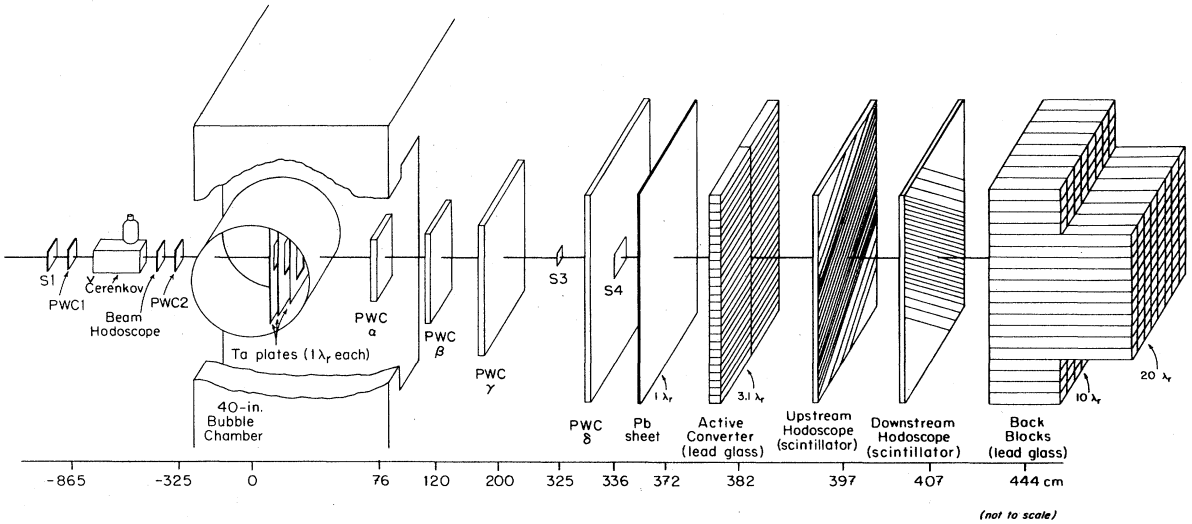

FIG. 1. The experimental setup. The beam travels from left to right.

electromagnetic-shower development at the scintillator hodoscope located between the active converter and absorber blocks. The hodoscope consisted of two planes each of 106 scintillator elements inclined at angles of 45° from the horizontal and mounted on $\frac{3}{4}$-in. plywood sheets. The middle 78 elements were 1.5 cm wide, while the 14 elements at both ends of each plane were 3 cm wide. The function of the hodoscope was to more accurately determine the centroid of showers initiated in the active converter.

The entire lead-glass-wall assembly was housed in a light-tight, air-conditioned plywood box which moved on rails mounted perpendicular to the beam. Thermistors inside the box measured the temperature for the temperature-dependent phototube gains.

In order to efficiently convert wide-angle γ rays, the bubble chamber was outfitted with three tantalum plates, each of 1-radiation-length thickness. Increasingly larger rectangular holes which covered the same solid angle as that subtended by the lead-glass wall from the center of the bubble-chamber of fiducial volume were cut in the plates. The bubble chamber, equipped with the plates, was pulsed at 12 Hz.

The bubble-chamber cameras were triggered when energy was detected by the lead-glass wall (fast trigger) and when the interaction could be determined from extrapolation of the PWC hits by on-line computer software (slow trigger) to not lie outside the fiducial volume. Each of the EMI 9618R phototubes in the lead-glass wall had an output at the last dynode stage which was fed to fast linear adders for an energy trigger TE. Thresholds were set so that 8 GeV gave an energy trigger with maximal efficiency. Thus the trigger was $S1 \cdot CB \cdot BH \cdot TE \cdot \overline{(S3+S4)}$.

All of the anode signals from the active converter and absorber blocks and 108 channels of the hodoscope were digitized by a 320-channel large-scale digitizer.[4] The remaining 104 hodoscope elements were digitized by LeCroy 2248 analog-to-digital converters (ADC's). Because of the relatively slow response of the lead glass an ADC integration time of 260 nsec was used and events were vetoed when S1·BH recorded another beam track within -150 to $+250$ nsec.

The software trigger was provided by a Data General NOVA 840 computer, operating in a foreground/background mode. The purpose of this software trigger was to increase the likelihood that the triggered event would lie inside the bubble-chamber fiducial volume. This trigger worked in a veto mode as a vertex could not be computed for every event.

The background software monitored the performance of the lead glass and associated electronics. Five monitoring procedures[5] were carried out during the runs: (1) A high-voltage monitor using LeCroy 2132 CAMAC interface unit connected to the LeCroy 4342 32-channel high-voltage power supplies. (2) A monitor of phototube gain changes using a single light-emitting diode (LED) (Monsanto MV5352) illuminating a bundle of optical light fibers (DuPont PFX0715) which were connected to individual lead-glass blocks. Between the LED and the fiber optics was a wheel of ten different neutral density filters which reduced the light intensity by known amounts. (3) A radioactive-source monitor consisting of ^{241}Am imbedded in a NaI crystal which was used to check output-level changes in the LED. A source and a fiber-optic cable were also attached to each of three reference counters consisting of lucite light pipes to which photomultiplier tubes were connected. (4) An ADC pedestal monitor which continually examined ADC pedestals between beam spills during the run. (5) A linearity monitor or digital-to-analog converter (DAC) which fed each ADC channel a known voltage and was used to correct any nonlinearities. As a result of these monitoring procedures, the energy calibration of the lead-glass array was followed throughout the experiment to an accuracy of 3%.

The calibration of the lead-glass wall was performed by exposing each block to electron beams of various known energies. The bubble-chamber magnet swept the beam in the vertical direction to impinge each block in a column and the wall was translated perpendicular to the beam along rails to position a new column in front of the beam.

The calibration relates the energy deposition in each block to the ADC reading for the photomultiplier attached to that block. Because the electron beam had to traverse the bubble chamber, the entrance and exit windows, and various scintillation counters and PWC's, the beam suffered considerable bremsstrahlung and was thus spread in energy and position at the lead-glass wall. For the calibration only blocks with at least 1% of the electron energy were used (typically 10 blocks). A χ^2 function was minimized in an iterative procedure in order to determine the gain of each block. Events with too low energy (below 95%) because of excessive bremsstrahlung or too much energy (above 110%) due to beam pileup were eliminated.

The energy resolution of the lead-glass array is a difficult parameter to extract and depends crucially on the running conditions. Tests in which an electron beam was directed onto a double-thickness lead-glass block gave $\sigma_E/E = 5.1\%/\sqrt{E}$ (energy in units of GeV) in agreement with the value quoted by the Particle Data Group.[6] In the later analysis of the two-π^0 data a resolution $\sigma_E/E = 12.5\%/\sqrt{E}$ was found to be necessary based on a study of fully constrained kinematics fits.

III. EVENT RECONSTRUCTION AND DATA ANALYSIS

The experiment consisted of 677 000 bubble-chamber photographs which contained 180 000 events. Approximately 73% of the photographs were taken under the trigger conditions, the remainder being taken under looser trigger conditions such as with an interacting beam trigger or in an untriggered mode in order to calculate cross sections and acceptances. This analysis is based on 30 242 triggered two-prong events.

Events were reconstructed in the following manner: The bubble-chamber film was scanned for all events inside the fiducial volume ($\sim$50 cm) unless the beam PWC's could not identify the interacting beam track, the lead-glass data was not usable, or the energy deposited in the lead glass was significantly less than that nominally required in the trigger film. These events were measured on manual or automatic measuring machines. Showers were identified in the lead-glass array and the resulting four-vector output merged with the bubble-chamber reconstructions. Finally, kinematic fitting was performed on the merged output. The film was rescanned for bubble-density information in order to identify the recoiling protons and reduce the number of kinematic ambiguities.

The shower-reconstruction program found clusters of energy in each part of the wall separately, then associated these energy clusters to make showers. Hot spots in the absorber blocks were defined as having more energy deposited than any of their neighbors. Each neighboring block was associated with the hot spot unless, as a diagonally related block, it had more energy deposited than the sum of the energies in the two adjacent nondiagonal neighboring blocks. In this case it formed a separate hot spot. In many cases blocks were neighbors of two or more hot spots and the energy in these blocks was partitioned in proportion to the energy of each hot spot association and inversely as the square of the distance from each hot spot. Hot spots in the active converter blocks were identified by a similar algorithm, except that the two columns of the active converter were treated independently of each other.

Showers in the hodoscope were identified by examining successive elements for signals that were at least two ADC counts above pedestal values. Each such consecutive element was included in the same showers until three adjacent elements with signals below threshold were encountered. Showers in the hodoscope were split in two if three adjacent elements could be found whose ADC total count was less than half of the total count of the three-element group on either side of it. The showers found in each hodoscope plane were matched with each shower in the other plane in order to define the possible location in space of all the showers.

A straight line was extrapolated from the main event vertex to the shower centroid in each part of the lead-glass wall. The closest showers in the active converter, absorber, and hodoscope, respectively, lying within 16, 15, and 7.5 cm were associated as components of a single shower. The spatial resolution of showers with hodoscope associations was estimated to be 2.0 cm, compared to 4.7 cm for those showers whose position was determined from the absorber blocks alone.

It was not always possible to make a complete association between showers in the various components of the lead-glass wall. The classification scheme shown in Table I gives the definition of each class and the number of occurrences of each class. Class 6 showers could arise because the active converter subtended a larger solid angle than the rest of the wall, class 4 showers can occur from neutral hadron interactions or as remnants of a previous

TABLE I. Definitions of shower classes and their respective numbers. There was a grand total of 65 285 showers in all two-prong, tight-trigger data. AC, active converter; HODO, scintillator hodoscope; BB, back block.

Class	AC	HODO	BB	No. of showers	Percent of total
1	×	×	×	25 526	39.1
2		×	×	2 152	3.3
3	×		×	11 080	17.0
4			×	10 772	16.5
5	×	×		1 898	2.9
6	×			11 158	17.1
7		Charged particles		2 699	4.1

interaction.

All showers were assumed to be γ-ray conversions. However, for a π^0 of energy greater than 3 GeV, the two decay γ rays would often not be resolved as two showers by the lead-glass wall. Therefore, a π^0 mass was also allowed for all showers with at least 3-GeV energy. Figure 2 shows the $\gamma\gamma$-mass distribution from all class 1 showers. The lower histogram shows the mass distribution when each shower has less than 3-GeV energy. The π^0 peak becomes more pronounced because some unresolved π^0 showers have been removed. The solid curve is a fit to a Gaussian plus polynomial background and gives a π^0 mass of 131 ± 3 MeV/c^2 with a σ of 55 ± 5 MeV/c^2.

Figure 3 displays the difference ΔE between the energy missing from the bubble chamber and that detected by the lead-glass wall. The events which make up the data sample of the lower histogram have no γ rays converting in the plates, so that in principle all the missing energy would be detected by the lead glass. Because of the finite solid angle, some γ rays miss the wall as well as the tantalum plates and, though the distribution peaks near zero with full width at half maximum of 2 GeV, the mean value is 0.8 GeV. Approximately 27% of the events have an energy difference greater than 2.5 GeV indicating that many of the kinematic fits will not be fully constrained. On the other hand, the existence of events with ΔE much less than zero energy implies that some events have extra showers in the wall, resulting from hadronic secondary interactions in the exit window or from occasional failure of the pileup veto. These showers are eliminated prior to kinematic fitting.

Because the γ rays from the π^0 decays corresponding to reaction (1) can convert in the liquid, lead glass, or plates or escape detection altogether the number of kinematic constraints can range from 1 to 8. Liquid γ-ray conversions and wall conversions were treated in a similar manner by the kinematics program. Often, many fits to reaction (1) were possible and the π^0 effective mass did not really constrain the primary vertex more than a single unresolved π^0 shower. In order to decide between competing ambiguous fits which might have the same number of kinematic constraints, a technique was developed to rate the quality of the fits. The actual algorithm used to select the best hypothesis was quite involved and is described in detail in Ref. 7.

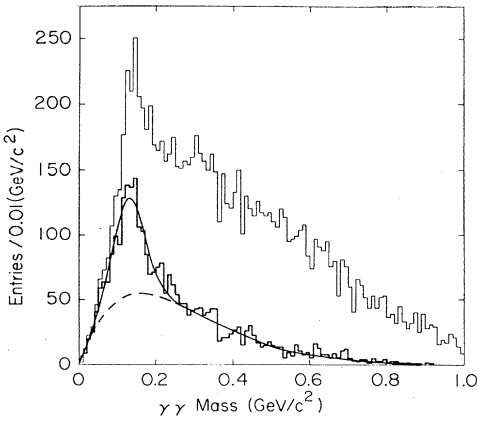

FIG. 2. γ-γ invariant masses for class 1 showers. The lower histogram also requires the two-shower energy to be less than 3 GeV. The solid curve is a fit to a Gaussian for the π^0 plus a polynomial background.

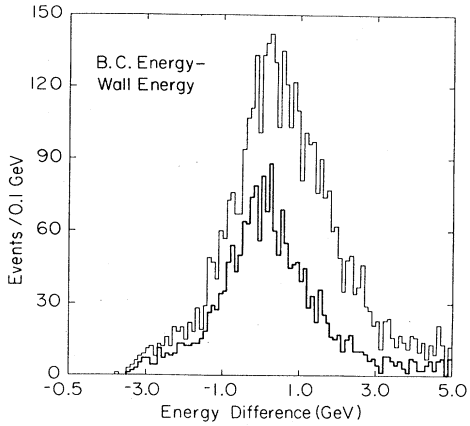

FIG. 3. Energy missing from the bubble chamber minus energy deposited in the wall. Upper curve is for all events and lower curve is for events with no plate γ's.

Because of secondary interactions and other beam-related phenomena, the presence of background showers was unavoidable. The actual algorithm for fit selection applied a weighting scheme which maximized the number of γ conversions used in the best fit while minimizing the excess energy deposited in the wall. The azimuth, dip, and curvature pull quantities for γ's and π^0's used in these best fits are distributed normally about zero and have standard deviations near one, indicating reasonable error estimates for the lead-glass generated showers. Figure 4 shows the confidence-level distribution for fits to reaction (1). The distribution is reasonably flat for confidence levels above 10%.

The finite solid angle subtended by the γ-ray converters required that acceptance calculations be performed. Weights for each event were obtained by moving the event to five different locations along the beam line, rotating the event about the beam line to 15 different angles and al-

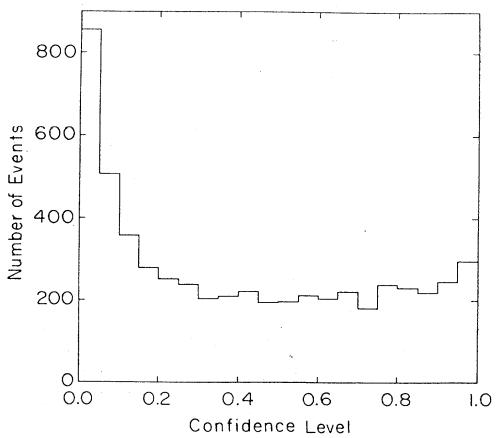

FIG. 4. Confidence levels of the best fits to reaction (1).

lowing 50 random π^0 decays at each orientation. The γ rays were tracked along straight lines through the apparatus to see if they struck the plates, the lead glass, or missed them both. Ten percent of the γ rays, the expected fraction, were randomly converted in the exit window of the bubble chamber to see if shower electrons would strike S3 and S4 and veto the event or if there was insufficient energy deposited in the lead-glass wall to satisfy the trigger. The weight for each event was thus

$$\text{weight} = \frac{3750}{\text{accepted events}} .$$

The acceptance is the reciprocal of the weight. As a check on this method of finding the acceptance, events corresponding to the reaction

$$\pi^+ p \rightarrow \Delta^{++}(1232) f^0(1270) ,$$

$$\Delta^{++} \rightarrow p\pi^+ ,$$

$$f^0 \rightarrow \pi^0\pi^0$$

were generated by a Monte Carlo program with an e^{10t} distribution, where t is the square of the four-momentum transfer from p to Δ^{++} and with a pure D-wave $f^0(1270)$ decay. The γ rays and charged tracks were propagated through the bubble chamber and downstream apparatus in the same fashion as was the real data. The average acceptance for the real data corresponding to the reaction $\pi^+ p \rightarrow \Delta^{++} f^0$ was found to be $(90 \pm 5)\%$, in reasonable agreement with the Monte Carlo–generated events.

IV. RESULTS ON $\pi^+ p \rightarrow \Delta^{++}\pi^0\pi^0$

A total of 30 242 two-prong events were measured in the triggered film. Of these events 17 610 with at least 3 GeV missing from the bubble chamber were passed through the kinematic program. Two cuts were applied to the data. Events with less than 7-GeV missing energy were removed as these events did not satisfy the hardware trigger. Also removed were events where more than 20-GeV neutral energy was deposited on the lead-glass detector. After performing kinematic fits 5139 events had their best fit to reaction (1). Each event was checked for charge-particle ionization identification to be consistent with the fit. For events with proton momentum greater than 1.2 GeV/c the ionization identification was ambiguous and so were removed from the sample leaving 3676 events fitting reaction (1). Figures 5 and 6 show the $\pi^0\pi^0$ and $\pi^+ p$ mass distributions, respectively. Clearly f^0 and $\Delta^{++}(1232)$ are seen in these two plots.

In order to understand the amount of background in reaction (1), Fig. 7(a) shows the square of the missing mass distribution recoiling against the $\pi^+ p$ and in Fig. 7(b) the $\pi^+ p$ is constrained to be Δ^{++} [mass $(\pi^+ p) < 1.35$ GeV/c^2]. Figure 8 shows the two-dimensional $\pi^+ p$ mass versus $\pi^0\pi^0$ mass for approximately half the data. The f^0 is clearly observed only for events with a Δ cut as seen both in Figs. 7 and 8. This is easy to understand because for $\Delta^{++}\pi^0\pi^0$ events, the π^+ and proton have low momentum and are swept out by the bubble-chamber magnet and cannot cause secondary interactions which can produce

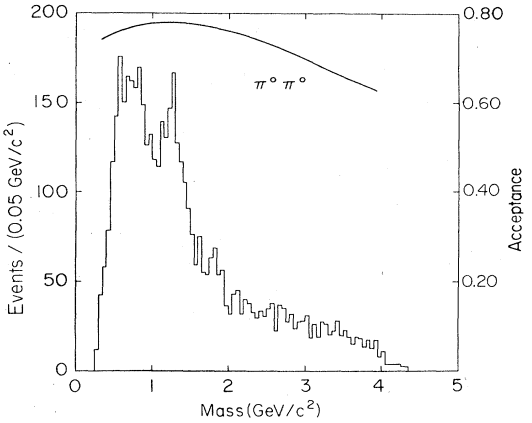

FIG. 5. $\pi^0\pi^0$ invariant mass for all events fitting reaction (1). The curve is the calculated acceptance.

more π^0's. In addition for $\pi^0\pi^0$ masses below 1.9 GeV/c^2 both π^0's will go toward the lead-glass detector and will be measured with better resolution as the π^0's have more than 14-GeV energy. We do not know how bad the contamination is for non-Δ events, but we are confident that the sample for reaction (2) (905 events) is essentially free of background. The clear f^0 peak in Fig. 7(b) reenforces our claim that the $\Delta^{++}\pi^0\pi^0$ have little background. We estimate that about 10% of the events in the $\pi^0\pi^0$ peak centered at zero in Fig. 7(b) are due to misidentified single π^0's and η's.

The $\pi^0\pi^0$ mass distribution corresponding to fits to reaction (1) as shown in Fig. 5 has the f^0 peak at 1.25 GeV/c^2. The broad low-mass enhancement is primarily associated with A_1^+ and A_2^+ which decay to $\rho^+\pi^0$ or with a Deck-type mechanism.[8] The curve represents the acceptance, calculated as described in the previous section. The 3π mass distribution with Δ^{++} removed is shown in Fig. 9 which has a prominent enhancement at a mass of 1.7 GeV/c^2, identified as the A_3. Figure 10 shows the acceptance-corrected $\pi^0\pi^0$ mass distribution for reaction (2). The acceptance correction is small, varying between 5% and 20%.

The advantage of $\pi^+ p \rightarrow \Delta^{++}\pi^0\pi^0$ reaction as an example of $\pi\pi$ scattering is that the S-wave amplitude can be studied without P-wave interference. Because of the

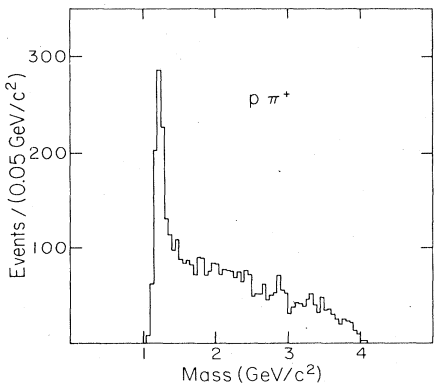

FIG. 6. $p\pi^+$ invariant mass for all events fitting reaction (1).

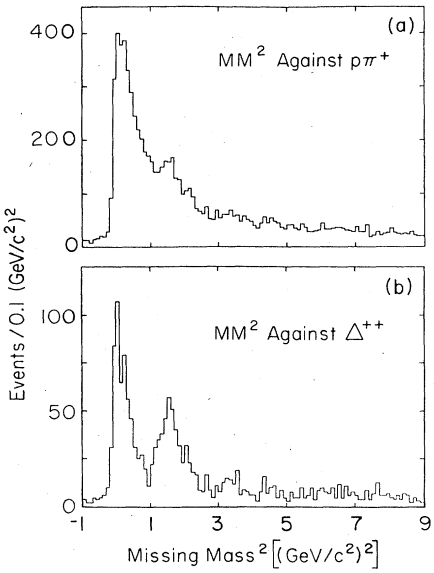

FIG. 7. Missing mass squared for two-prong events with proton momentum <1.2 GeV/c. (a) All events, (b) mass $(p\pi^+)<1.35$ GeV/c^2.

trigger-energy requirements a cross section which can be compared to other experiments for many reactions is difficult to obtain. Fortunately, events corresponding to reaction (2) would almost always trigger the bubble-chamber cameras. In order to carry out this cross-section calculation, data was taken in an untriggered mode. Using this data we established our cross-section normalization[9] for process x with

$$\sigma_x=(0.048\pm0.003)N_x\eta_x{}^{-1}\ \mu\text{b}\ . \tag{3}$$

The charged-particle efficiency η_x is the product of the scanning efficiency (0.98±0.01), measuring efficiency (0.79±0.01), kinematic reconstruction efficiency (0.98±0.01), and a factor (0.90±0.03) to correct for the cuts made in the data sample before measuring (no secondary interactions and no Dalitz pairs). The number of events, N_x, must be corrected for acceptance as well as detection efficiency.

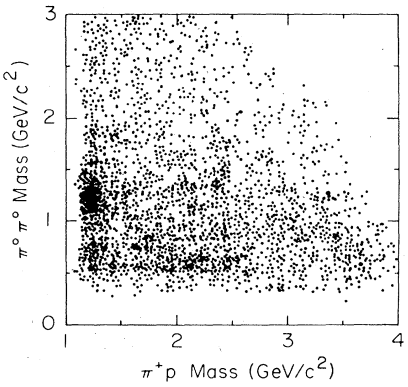

FIG. 8. $\pi^0\pi^0$ mass versus π^+p mass for events fitting reaction (1). Only one-half of data is presented.

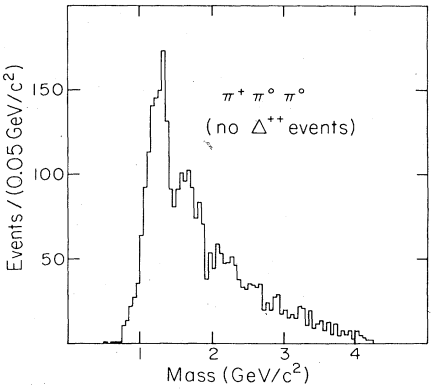

FIG. 9. Three-pion invariant mass for events fitting reaction (1) with the events with π^+p mass <1.35 GeV removed.

The acceptance for Monte Carlo–generated events corresponding to reaction (2) was obtained in a manner similar to that described in Sec. III. The Δ^{++} was assumed to have an e^{10t} distribution and 7-GeV energy was required to be deposited in the lead glass. The average acceptance was found to be 85%. The cross section for the reaction $\pi^+p\to\Delta^{++}f^0(1270)$, $f^0\to\pi^0\pi^0$ was obtained by integration of a fitted Breit-Wigner form to the $\pi^0\pi^0$ mass spectrum between 0.75 and 1.75 GeV/c^2. The 365±40 events have a cross section of 25.8±3.4 μb. The background was represented by a Gaussian with standard deviation equal to 0.23±0.02 GeV/c^2 centered at 0.65±0.02 GeV/c^2 plus a polynomial of the form $Am^\alpha(1-m)^\beta$, where

$$m=(m_{\pi\pi}-m_{\pi\pi\,\min})/(m_{\pi\pi\,\max}-m_{\pi\pi\,\min})\ .$$

The mass and width of the f^0 from the Breit-Wigner fit were found to be 1.25±0.01 and 0.23±0.02 GeV/c^2, respectively. The mass is somewhat lower and the width somewhat greater than the accepted values of 1.27 and 0.18 GeV/c^2, respectively.[6] Table II shows the cross section for this reaction obtained by this and other experiments of comparable beam energies.

The Gottfried-Jackson scattering angle in the $\pi^0\pi^0$ center-of-mass system is shown in Fig. 11 for three mass

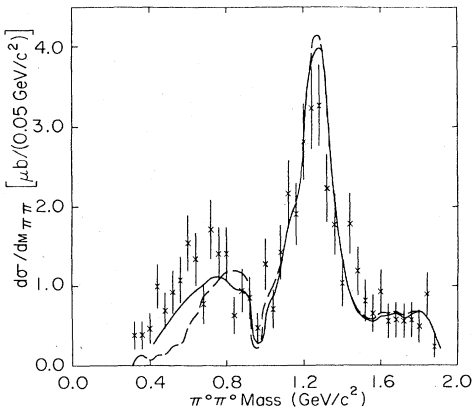

FIG. 10. $\pi^0\pi^0$ invariant-mass distribution. Curves are one-pion-exchange predictions, dashed using solution A and solid using solution B.

TABLE II. Cross sections for the reaction $\pi^+p\to\Delta^{++}f^0$ measured by various experiments at beam energies near 16 GeV.

Expt.	Beam momentum (GeV)	$\sigma(\pi^+p\to\Delta^{++}f^0)$ (μb)
This expt.	15.7	77±12
Ballam *et al.* (Ref. 10)	16	99±21
Deutschmann *et al.* (Ref. 11)	16	98±12
Gaidos *et al.* (Ref. 12)	13.1	115±7
Biswas *et al.* (Ref. 13)	18.5	41±10

regions. The unweighted events are shaded. For reaction (2) there are no holes in the acceptance. The unnormalized moments $N\langle Y_L^M\rangle$, where Y_L^M is the spherical harmonic in the Gottfried-Jackson frame and N the number of events, are plotted in Fig. 12 as a function of $\pi^0\pi^0$ mass. Only the Y_L^0 moments are nonzero indicating that reaction (2) is dominated by pion exchange. Only S and D waves appear to be present and below a $\pi^0\pi^0$ mass of 1 GeV/c^2 only S wave is present. The moments can be rewritten in terms of the amplitudes:

$$\begin{aligned}\langle Y_0^0\rangle &= |S|^2+|D|^2\,,\\ \langle Y_2^0\rangle &= 2S^*D+(2\sqrt{5}/7)|D|^2\,,\\ \langle Y_4^0\rangle &= (\tfrac{6}{7})|D|^2\,.\end{aligned}\tag{4}$$

Our data are not sufficient to determine the production amplitudes as functions of t, extrapolate in t to the pion pole, and calculate the phase shifts from the extrapolated amplitudes. However, the amplitudes can be computed following a procedure similar to that of Apel[14] by using the phase shifts determined in other experiments. We can then compare these predictions to our data. With only S and D waves present, the angular distribution is given by

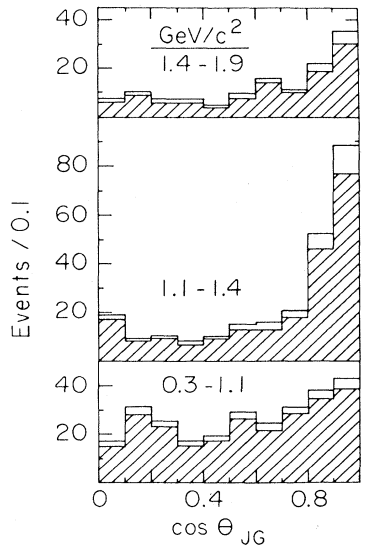

FIG. 11. Unweighted (shaded) and weighted distributions of $\cos\theta_{JG}$ (Jackson-Gottfried) angle for three $\pi^0\pi^0$ mass regions.

$$\frac{dN}{dM_{\pi\pi}d\cos\theta}=C_N\frac{M\pi\pi}{q}[\,A_0(M_{\pi\pi})Y_0^0+A_2(M_{\pi\pi})Y_2^0(\cos\theta)+A_4(M_{\pi\pi})Y_4^0(\cos\theta)]\,,\tag{5}$$

where the angular distribution has been integrated over the azimuthal angle, q is the π^0 momentum in the $\pi^0\pi^0$ center of mass, and C_N is a normalization constant.

The data with $|t|<0.27$ (GeV/c)^2 were divided into seven mass regions and the angular distributions fitted to determine the A_L assuming the D wave was given by a relativistic Breit-Wigner form with mass $=1.27$ GeV/c^2 and width$=0.18$ GeV/c^2 and effective-range parameter $R=1$ in the centrifugal barrier function. Table III lists the values of

$$f_S=|S|^2/(|S|^2+|D|^2)\,,$$

the S-waves fraction, and cos(SD), the cosine of the angle between the S- and D-wave amplitudes. Figure 13(a) shows f_S (solid circles) and the S-wave cross section (open circles); Fig. 13(b) shows cos(SD). Below $M_{\pi\pi}\sim0.9$ GeV/c^2 f_S is approximately equal to one, above the KK threshold f_S drops to about 0.5 and stays low through $M_{\pi\pi}\sim1.4$ GeV/c^2 as the D wave becomes significant. Substantial S wave exists up to $\pi^0\pi^0$ mass for 1.5 GeV/c^2, coupled with the relatively constant cos(SD) in the region of the D-wave resonance, $f^0(1270)$. Several other experiments have studied the same reaction, and in particular, the results of Apel *et al.*[14] and Cason *et al.*[15] are quite similar to ours. Owing to the limitation of our statistics we do not observe the 1.5 GeV/c^2 S-wave dip as reported in Refs. 14 and 15, but we do observe the S-wave cross section dropping by a factor of 3 from $M(\pi\pi)$ of 1.2 to 1.6 GeV/c^2 as seen in Fig. 13(a). The analysis of Biswas *et al.*[16] at a beam momentum of 8 GeV/c, resulted in $|S|^2$ being much smaller than observed here for $M_{\pi\pi}<0.6$ GeV/c^2. This observation is also reflected in the phase-shift analysis of $\pi\pi$ scattering, which we discuss below.

The spin-averaged π^+p scattering cross section mediated by pion exchange with Δ^{++} formation at the lower vertex can be written in the form

$$\frac{d\sigma}{d\Omega\,dt\,dS_{12}}=\frac{1}{2\pi}\frac{G^2}{4\pi}\frac{|V|^2}{(t-M_p{}^2)^2}\frac{|f_{\pi\pi}|^2}{4Sq_0}\times S_{12}[1-(4M_\pi{}^2/S_{12})]^{1/2}\,,\tag{6}$$

where $f_{\pi\pi}$ is the $\pi\pi$ scattering amplitude, $|V|^2$ is the

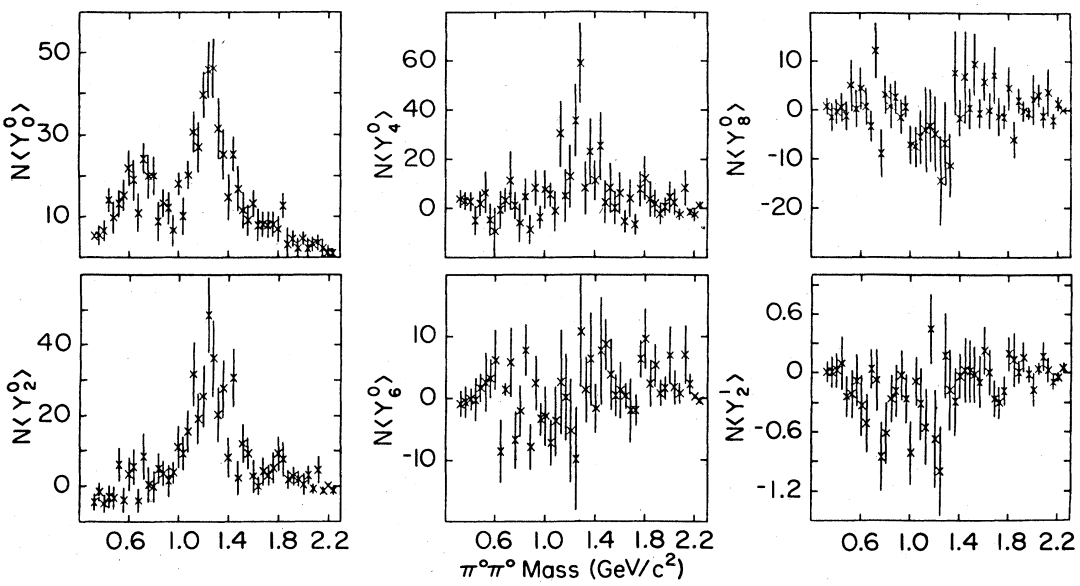

FIG. 12. Unnormalized moments of the $\pi^0\pi^0$ system in the Gottfried-Jackson reference frame.

sum squared of the possible Δ vertex factors for each possible helicity flip, G is the $\pi N\Delta$ coupling constant, t is the four-momentum transfer squared, S and S_{12} are, respectively, the square of the overall and $\pi\pi$ center-of-mass energies, and q_0 is the incident center-of-mass momentum. For a derivation of expression 6, see Ref. 7. The amplitude $f_{\pi\pi}$ can be written in the form

$$f_{\pi\pi}=\frac{1}{k}\sum\sum C_I(2L+1)f_L^I P_L(\cos\theta)\ , \tag{7}$$

where I is the isospin of the $\pi\pi$ system, C_I ($=-\frac{1}{3}$ for $I=2$, $+\frac{1}{3}$ for $I=0$) is the isospin factor, L is the angular momentum, and P_L is the Lth-order Legendre polynomial of cosine of the Jackson angle of one π^0. The amplitude f_L^I, written in terms of the phase shift, is

$$f_L^I=\sin(\delta_L^I)\exp(i\delta_L^I)\ . \tag{8}$$

Empirically, in amplitude calculations it has been found necessary to multiply $f_{\pi\pi}$ by an $\exp[b(t-M_{\pi\pi}{}^2)]$ form factor, where b is determined from fitting the data. The same procedure was applied to these data.

For $\pi\pi$ masses below 1 GeV/c^2 where the S wave is dominant, two sets of $I=0$ phase shifts, A and B, were

TABLE III. Results of the amplitude analysis for the reaction $\pi^+p\to\Delta^{++}\pi^0\pi^0$ where $f_S=|S|^2/(|S|^2+|D|^2)$ is the fraction of S wave and cos(SD) is cosine of angle between the S and D waves. (a) For events with $|t|<0.27$ (GeV/c)^2. (b) For events with $|t|<0.12$ (GeV/c)^2.

$\pi^0\pi^0$ mass (GeV/c^2)	f_S	cos(SD)
	(a) $\|t\|<0.27$ (GeV/c)^2	
0.3–0.6	0.982±0.074	−0.25±0.37
0.6–0.9	0.949±0.027	0.61±0.21
0.9–1.1	0.607±0.079	0.32±0.13
1.1–1.25	0.573±0.046	0.636±0.072
1.25–1.4	0.336±0.033	0.38±0.10
1.4–1.6	0.507±0.066	0.41±0.12
1.6–1.9	0.799±0.078	0.46±0.17
	(b) $\|t\|<0.12$ (GeV/c)^2	
0.3–0.6	0.990±0.015	
0.6–0.9	0.93±0.12	0.74±0.20
0.9–1.1	0.52±0.08	0.35±0.15
1.1–1.25	0.57±0.06	0.70±0.10
1.25–1.4	0.46±0.07	0.56±0.11
1.4–1.6	0.24±0.03	0.44±0.22
1.6–1.9	0.70±0.11	0.73±0.19

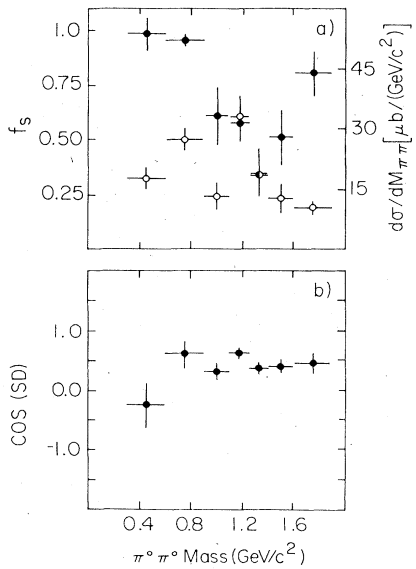

FIG. 13. Results of the amplitude analysis for $|t|<0.27$ (GeV/c)^2. (a) f_S is fraction of S wave represented by solid circles. Open circles represent S-wave cross section. (b) The cosine of the angle between S and D waves.

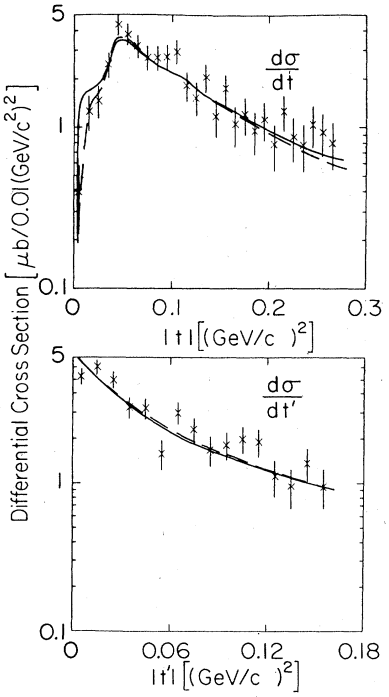

FIG. 14. One-pion-exchange prediction for $d\sigma/dt$ and $d\sigma/dt'$ using solution A (solid curve) and solution B (dashed curve) phase shifts.

considered. The first and most recent phase shifts (solution A) of Biswas *et al.*[16] were determined in a streamer-chamber investigation of the reaction $\pi^+p\to\Delta^{++}\pi^0\pi^0$ at 8 GeV/c. The second set of δ_0^0 phase shifts (solution B) were determined by Estabrooks and Martin[17] from data taken by the CERN-Munich Collaboration[18] studying the reaction $\pi^-p\to\pi^+\pi^-n$ at 17.2 GeV/c.[19] For the $I=2$ S-wave phase shift δ_0^2 when working with solution A we used the same parametrization of the results of Hoogland *et al.*[20] as employed by Biswas *et al.*,[16] namely,

$$\delta_0^2=\frac{-1}{1.1+0.884q}\ , \tag{9}$$

where q is the π^0 momentum in GeV/c in the $\pi^0\pi^0$ center of mass and δ_0^2 is in radians. When using solution B we inputted for δ_0^2 the tabulated values of Estabrooks and Martin,[17] which are slightly less negative than those implied by Eq. (9).

Above $M_{\pi\pi}=1$ GeV/c^2 the D wave becomes significant. The δ_2^0 phase shift was obtained by equating the $\exp(i\delta_2^0)\sin(\delta_2^0)$ to a relativistic Breit-Wigner resonance form for the f^0 with mass 1.27 GeV/c^2 and width 0.18 GeV/c^2 with the effective-range parameter R set equal to 1. The δ_2^2 phase shifts in this mass range were measured by Hoogland[20] to be near zero and were thus ignored. The $\delta_0^2=8.8-30M_{\pi\pi}$, where δ_0^2 is in degrees and $M_{\pi\pi}$ in GeV/c^2.

Figure 10 shows the $\pi^0\pi^0$ mass distribution against the Δ^{++} [$M(\pi^+p)<1.35$ GeV/c^2]. The curves are the one-pion-exchange predictions using the phase shifts from solutions A and B just described. The curves were generated by numerically integrating Eq. (6) over the appropriate variables and performing a least-squares fit simultaneously to $d\sigma/dM_{\pi\pi}$ and $d\sigma/dt$. Two parameters, the overall normalization and the constant b in the exponential form factor, were used. The fit using solution B phase shifts gave much better agreement with our data [$b=1.12\pm0.14$ (GeV/c)$^{-2}$ and $\chi^2/\mathrm{DF}=1.2$] than did solution A phase shifts [$b=1.51\pm0.12$ (GeV/c)$^{-2}$ and $\chi^2/\mathrm{DF}=1.9$]. The primary discrepancy with solution A is in the low-mass region where the cross-section predictions are much too low. Possible η or ω^0 contamination in our data is too small to account for this difference. Solution A phase shifts are simply lower than those of other determinations for $\pi\pi$ masses below 1 GeV.

The t and t' ($t'=t-t_{\min}$) distributions are shown in Fig. 14 along with the computations of solutions A and B. Events plotted here had $\pi^0\pi^0$ masses less than 1.9 GeV/c^2. The t' distributions can be described by a simple exponential with a slope parameter of 11.1 ± 0.7 (GeV/c)$^{-2}$. The two phase-shift solutions A and B are clearly equally satisfactory in describing t and t' distributions of our data.

V. SUMMARY

A lead-glass array has been used in conjunction with the 40-in. rapid-cycling bubble chamber to reconstruct events of the type $\pi^+p\to\pi^+p\pi^0\pi^0$. With a sensitivity of 14.2 events/μb the $\pi^0\pi^0$ invariant-mass distribution showed no evidence for neutral mesons with mass between the $f^0(1270)$ and 3 GeV. An analysis of the reaction $\pi^+p\to\Delta^{++}\pi^0\pi^0$ with $|t|<0.27$ (GeV/c)^2 showed that the $\pi^0\pi^0$ system below a mass of 1 GeV/c^2 was pure S wave and that, while the D-wave $f^0(1270)$ dominated its mass region, substantial S wave exists in the mass region above 1 GeV/c^2. The amplitude analysis indicated that the ratio $|S|/|D|$ was independent of t.

The phase shifts obtained by Estabrooks and Martin[17] described the $\Delta^{++}\pi^0\pi^0$ data well, but the phase shifts of Biswas *et al.*[16] underestimated the $\pi^0\pi^0$ cross section below 1 GeV.

ACKNOWLEDGMENTS

We wish to thank the SLAC bubble-chamber group, especially R. C. Field, J. T. Carroll, and A. Leino for help in getting the experiment working. We also wish to acknowledge the help of C. Hoarde, L. Barker, W. Smith, P. Haridas, and J. Hargis. We gladly acknowledge J. F. Owens and J. D. Kimel for valuable discussions of the theoretical models used here. This work is supported in part by grants from the U. S. Department of Energy.

*Present address: NSPL Station, Bay St. Louis, Mississippi.
†Present address: RCA, Fort Walton Beach, Florida.
‡Present address: American Dade, Costa Mesa, California 92626.
§Present address: Science Applications, Inc., Sunnyvale, California 94089.
**Present address: SLAC, Stanford, California 94305.
††Present address: Fermilab, Batavia, Illinois 60510.

[1]J. E. Brau *et al.*, Nucl. Instrum. Methods **196**, 403 (1982).
[2]J. M. Feller *et al.*, Lawrence Berkeley Laboratory Report No. LBL-6466, 1977 (unpublished).
[3]R. C. Field, SLAC SHF Note No. 67, 1977 (unpublished).
[4]R. F. Althaus *et al.*, IEEE Trans. Nucl. Sci. **NS-24**, 218 (1977); **NS-24**, 408 (1977).
[5]Similar monitoring procedures are described by R. J. Madaras, B. Pardoe, and R. Pecyner, Nucl. Instrum. Methods **160**, 263 (1979).
[6]Particle Data Group, Phys. Lett. **111B**, 1 (1982).
[7]R. K. Clark, Ph.D. dissertation, Florida State University, 1983.
[8]E. L. Berger, Phys. Rev. **166**, 1525 (1968); G. Ascoli *et al.*, Phys. Rev. D **8**, 3894 (1973).
[9]T. Glanzman, Ph.D. dissertation, Duke University, 1982.
[10]J. Ballam *et al.*, Phys. Rev. D **4**, 1946 (1971).
[11]M. Deutschmann *et al.*, Phys. Lett. **19**, 608 (1965).
[12]J. A. Gaidos *et al.*, Nucl. Phys. **B26**, 225 (1971).
[13]N. N. Biswas *et al.*, Phys. Rev. D **2**, 2529 (1970).
[14]W. D. Apel *et al.*, Nucl. Phys. **B160**, 42 (1979); **B201**, 197 (1982).
[15]N. M. Cason *et al.*, Phys. Rev. Lett. **48**, 1316 (1982); Phys. Rev. D **28**, 1586 (1983).
[16]N. N. Biswas *et al.*, Phys. Rev. Lett. **47**, 1378 (1981).
[17]P. Estabrooks and A. D. Martin, Nucl. Phys. **B79**, 301 (1974).
[18]G. Grayer *et al.*, Nucl. Phys. **B75**, 189 (1974).
[19]There are important differences in the methods of phase-shift computations of Refs. 16 and 17. Biswas *et al.* compute via an extrapolation in t to the pion pole while Estabrooks and Martin performed an amplitude analysis of the observed moments of small-t events.
[20]W. Hoogland *et al.*, Nucl. Phys. **B69**, 266 (1974).